ACIN

Real-time closed-loop control for micro mirrors with quasistatic comb drives

Richard Schroedter[a], Thilo Sandner[a], Klaus Janschek[b], Matthias Roth[b], and Clemens Hruschka[a]

[a]Fraunhofer Institute for Photonic Microsystems (FhG-IPMS), AMS, Microscanner R&D, Dresden, Germany
[b]Institute of Automation, Faculty of Electrical and Computer Engineering, Technische Universität Dresden, 01062 Dresden, Germany

ABSTRACT

This paper presents the application of a real-time closed-loop control for the quasistatic axis of electrostatic micro scanning mirrors. In comparison to resonantly driven mirrors, the quasistatic comb drive allows arbitrary motion profiles with frequencies up to its eigenfrequency. A current mirror setup at Fraunhofer IPMS is manufactured with a staggered vertical comb (SVC) drive and equipped with an integrated piezo-resistive deflection sensor, which can potentially be used as position feedback sensor. The control design is accomplished based on a nonlinear mechatronic system model and the preliminary parameter characterization. In previous papers [1, 2] we have shown that jerk-limited trajectories, calculated offline, provide a suitable method for parametric trajectory design, taking into account physical limitations given by the electrostatic comb and thus decreasing the dynamic requirements. The open-loop control shows in general unfavorable residual eigenfrequency oscillations leading to considerable tracking errors for desired triangle trajectories [3]. With real-time closed-loop control, implemented on a dSPACE® system using an optical feedback, we can significantly reduce these errors and stabilize the mirror motion against external disturbances. In this paper we compare linear and different nonlinear closed-loop control strategies as well as two observer variants for state estimation. Finally, we evaluate the simulation and experimental results in terms of steady state accuracy and the concept feasibility for a low-cost realization.

Keywords: real-time closed-loop control, quasistatic microscanner, electrostatic staggered vertical comb drive, flatness-based and sliding-mode control, normal form and high-gain observer

1. INTRODUCTION

Micro scanning mirrors play an important role in various applications for highly miniaturized, reliable and cost efficient scanning systems like compact laser projection displays [4, 5], portable scanning grating spectrometers [6] or LIDAR [7]. These MEMS devices feature a low cost, CMOS compatible production process as well as high accuracy and high scan rate properties. Compared to Lissajous figure scanning followed by resonant 2D scanning systems [4], quasistatic microscanners can perform arbitrary trajectories or tilt statically with high precision and repeatability. The presented cardanic 2D quasistatic resonant scanner, Fig. 1, can realize a raster scan by combining a sawtooth motion of the outer quasistatic axis and a resonant motion of the inner resonant axis. The quasistatic axis of the 2D micro scanner, cf. Fig. 1b,1d, tilts electrostatically driven using a staggered vertical comb drive. This very low damped spring mass system has to be controlled to realize high precise tracking applications.

In previous works, we concentrated on open-loop control strategies [1, 3, 8]. In this contribution we compare and validate the real-time closed-loop control with a robust linear PID controller [9] and with nonlinear closed-loop control methods: flatness-based control as system inversion and sliding-mode control. The sliding-mode


Further author information: (Send correspondence to Richard Schroedter)
Richard Schroedter: E-mail: richard.schroedter@ipms.fraunhofer.de, Telephone: + 49 351 8823 196
Klaus Janschek: E-mail: klaus.janschek@tu-dresden.de, Telephone: +49 351 463 34025

control [10–12] achieves exceptional tracking performance by high frequency switching. The resulting characteristic chattering pose no problem for the micro mirror electrostatic comb drive. An external optical sensor serves for measuring the micro mirror tilt position. As an alternative to this optical feedback considered in this paper, recent technology developments in piezo-sensors show the potential to serve as an internal measurement for closed loop feedback control [13].

After introducing the system modeling and state of the art open-loop control techniques in section 2, we derive the closed-loop control strategies in section 3 and demonstrate the experimental results in section 4.
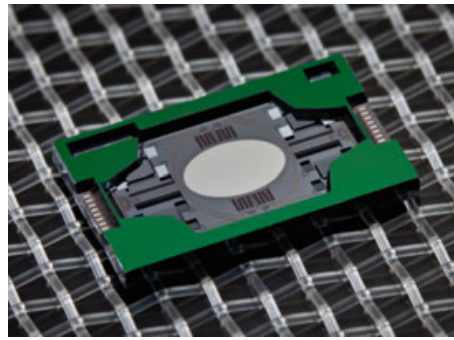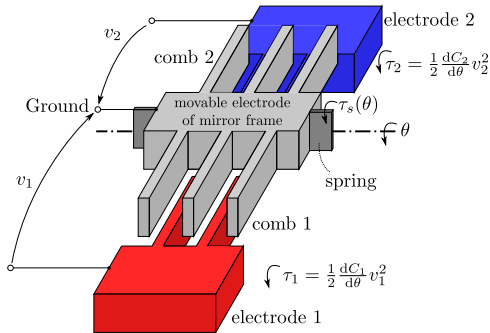

(a) Photograph of 2D quasistatic-resonant microscanner chip [14]; the mirror size is $2.6\,\mathrm{mm} \times 3.6\,\mathrm{mm}$
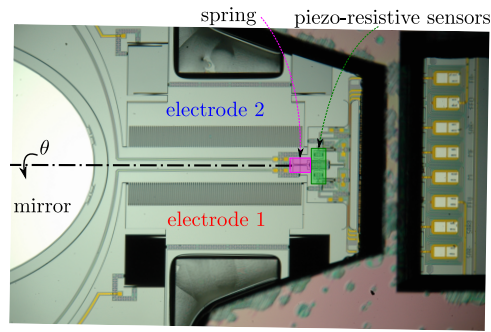
(b) Detailed photograph of quasistatic comb drive showing the arrangement of the comb electrodes, spring and the piezo-resistive sensor [15, 16]
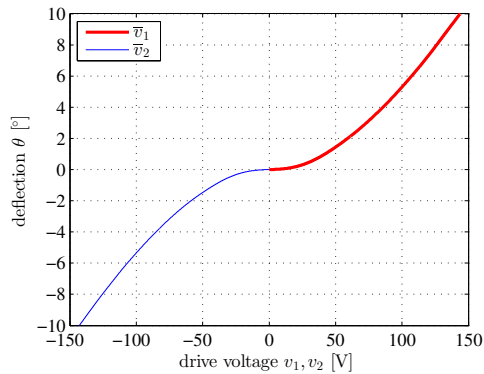
(c) Static voltage deflection characteristic $\overline{\theta}(\overline{v}_{1,2})$ up to max. deflection angle of $\pm 10\,^\circ$ with $\overline{v}_{1,\mathrm{max}} = 145\,\mathrm{V}$ for positive deflection $\theta > 0$ and $\overline{v}_{2,\mathrm{max}} = 143\,\mathrm{V}$ for negative deflection $\theta < 0$

(d) Principal design of quasistatic *staggered vertical comb* drive showing electrical connections and torques [1]

Figure 1: 2D quasistatic-resonant microscanner chip from TACO project [14]

2. OPEN-LOOP CONTROL OF QUASISTATIC COMB DRIVE

The control aims at generating the input voltages for tracking a desired deflection trajectory. Therefore we create a physical model of the mechatronic system, cf. Fig. 1d, and identify its parameters as follows. We suppose the

torque equilibrium Eq. (1), neglecting external disturbances:

$$J\ddot{\theta} + b\dot{\theta} + \tau_s(\theta) = \underbrace{\frac{1}{2}\frac{\mathrm{d}C_1}{\mathrm{d}\theta}v_1^2}_{\tau_1} + \underbrace{\frac{1}{2}\frac{\mathrm{d}C_2}{\mathrm{d}\theta}v_2^2}_{\tau_2},$$ (1)

where $\theta, \dot{\theta}, \ddot{\theta}$ denote the deflection angle and its time derivatives, v_1 and v_2 are the applied driving voltages at the comb electrodes, τ_1 and τ_2 describe the electrostatic drive torques and the mirror parameters are: mirror inertia J, linear viscous damping b, nonlinear spring torque $\tau_s(\theta)$, and the capacitance derivatives $\frac{\mathrm{d}C_{1,2}}{\mathrm{d}\theta} = C'_{1,2}(\theta)$. We determined the mirror inertia $J = 3.89 \times 10^{-12}\,\mathrm{kgm^2}$ with an ANSYS® finite element model. By exciting the mirror with an voltage impulse of 25V for 2ms and fitting the decay curve towards $\theta(t) = \hat{\theta}_0 e^{-D\omega_0 t}\cos\left(\sqrt{1-D^2}\omega_0 t\right)$, we identify the linear damping coefficient $b = 2JD\omega_0 = 5.091 \times 10^{-11}\,\mathrm{Nms}$ and the small signal stiffness $k_0 = J\omega_0^2 = J(2\pi f_0)^2$. The eigenfrequency is determined as $f_0 = 113.3\,\mathrm{Hz}$. The approximated nonlinear progressive stiffness $k(\theta)$ taken from an ANSYS® finite element model with the measured linear spring stiffness $k_0 = 1.972 \times 10^{-6}\,\mathrm{Nm/rad}$ (derived from small signal behavior around zero tilt position) is sketched in Fig. 2b, and the corresponding spring torque is determined by Eq. (2):

$$\tau_s(\theta) = \int_0^\theta k(\theta')\mathrm{d}\theta' - k(0) + k_0.$$ (2)

By evaluating the static voltage deflection characteristic $\overline{\theta}(\overline{v}_{1,2})$, cf. Fig. 1c, we compute the nonlinear electrostatic capacitances using Eq. (3), as shown in Fig. 2a [1]. For tilt deflections where the regarding comb is not engaged, we approximate the capacitance derivative with an exponential extrapolation.

$$C'_{1,2}(\overline{\theta}) = \frac{2\tau_s(\overline{\theta})}{\overline{v}_{1,2}^2(\overline{\theta})}$$ (3)

(a) Capacitance derivatives calculated with Eq. (3); the dashed curves are exponential extrapolations beginning from $\theta = 0$ [1]

(b) Progressive spring stiffness from ANSYS® finite element model, corrected with measured small signal spring stiffness k_0 around zero tilt position
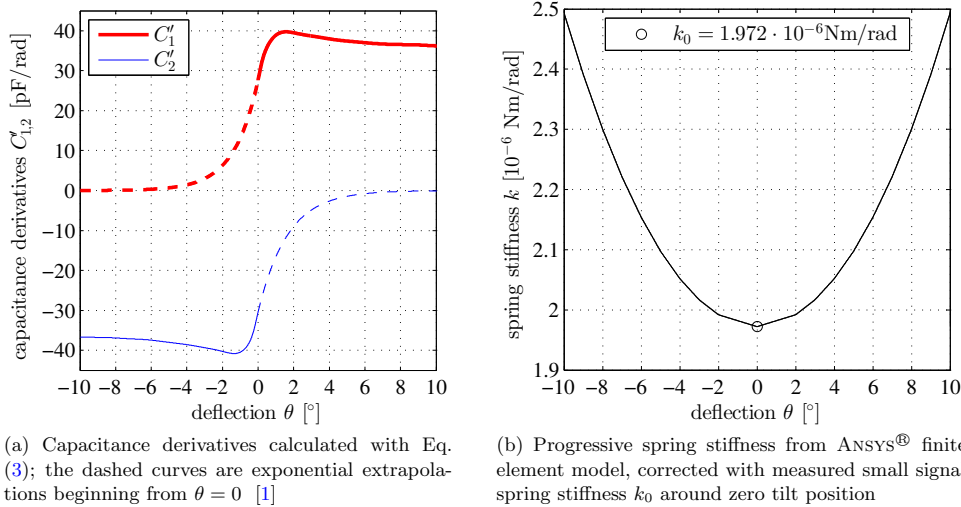
Figure 2: Model parameters for capacitance and spring stiffness

State space model From the torque equilibrium Eq. (1) we derive the state space model Eq. (4) [3] in the form $\dot{\boldsymbol{x}} = f(\boldsymbol{x}, u)$, using the state definition $\boldsymbol{x} := (x_1, x_2) = (\theta, \dot{\theta})$ with the output $y := x_1 = \theta$,

$$\dot{x}_1 = x_2 \tag{4a}$$

$$\dot{x}_2 = -\frac{b}{J}x_2 - \frac{\tau_{\mathrm{s}}(x_1)}{J} + u \tag{4b}$$

and defining a *generalized input* u as follows:

$$u := \frac{1}{2J}C_1'(\theta)v_1^2 + \frac{1}{2J}C_2'(\theta)v_2^2. \tag{5}$$

Jerk-limited trajectories Most raster scan applications require triangle trajectories or sawtooth trajectories. We apply jerk limited trajectories [1] as shown in Fig. 10, 11 for the nominal applications, because non-smooth trajectories lead to high oscillation of the very low damped spring mass system eigenmode [8]. We generate these trajectories by assembling segments of the polynomials Eq. (6), with the appropriate constants for each segment: maximum jerk $j_{\max} = \dddot{\theta}_{\max}$, start deflection θ_0, start velocity $\dot{\theta}_0$ and start acceleration $\ddot{\theta}_0$.

$$\theta_{\mathrm{d}}(t) = \theta_0 + \dot{\theta}_0 t + \frac{\ddot{\theta}_0}{2}t^2 + \frac{j_{\max}}{6}t^3, \qquad \dot{\theta}_{\mathrm{d}}(t) = \dot{\theta}_0 + \ddot{\theta}_0 t + \frac{j_{\max}}{2}t^2, \qquad \ddot{\theta}_{\mathrm{d}}(t) = \ddot{\theta}_0 + j_{\max}t \tag{6}$$

Open-loop control The open-loop control, cf. Fig. 3, is realized by inverting the parameterized system Eq. (4) and (5), as shown in [3]. First, we calculate the desired feedforward acceleration u_{d} of the generalized input by evaluating the second part of Eq. (4) with the desired trajectory $(\theta_{\mathrm{d}}, \dot{\theta}_{\mathrm{d}}, \ddot{\theta}_{\mathrm{d}})$:

$$u_{\mathrm{d}} = \frac{\tau_{\mathrm{s}}(\theta_{\mathrm{d}})}{J} + \frac{b}{J}\dot{\theta}_{\mathrm{d}} + \ddot{\theta}_{\mathrm{d}} \tag{7}$$

Second, a switch toggles between the comb electrodes according the sign of the desired generalized input u_{d} as follows:

$$v_1 = \begin{cases} \sqrt{\dfrac{2Ju_{\mathrm{d}}}{C_1'(\theta_{\mathrm{d}})}} & \text{for} \quad u_{\mathrm{d}} > 0 \\ 0 & \text{for} \quad u_{\mathrm{d}} \leq 0 \end{cases} \qquad v_2 = \begin{cases} 0 & \text{for} \quad u_{\mathrm{d}} > 0 \\ \sqrt{\dfrac{2Ju_{\mathrm{d}}}{C_2'(\theta_{\mathrm{d}})}} & \text{for} \quad u_{\mathrm{d}} \leq 0 \end{cases}. \tag{8}$$

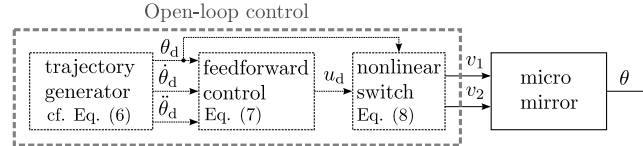All open-loop calculations can be processed offline.

Figure 3: Open-loop control structure with the feedforwad control part, Eq. (7), and the comb switch Eq. (8)

3. CLOSED-LOOP CONTROL

The open-loop control presented in section 2 cannot compensate model inaccuracies or external disturbances, like shock or long-term parameter drifts caused by temperature and pressure changes. For this reason we develop and compare three different closed-loop control strategies feeding back an online measurement of the actual mirror tilt deflection. We realize these feedback controller complemented by our open loop control explained above.

For further information contact: schroedter@acin.tuwien.ac.at, https://orcid.org/0000-0003-3259-4571

3.1 Linear control

As linear control law, we implement the robust PID controller [9] given with the Eq. (9) as a LAPLACE transform. This method influences directly the drive voltage for controlling the position error $e(s) = \theta_d - \tilde{\theta}$, defined as the difference between desired trajectory θ_d and measured tilt angle $\tilde{\theta}$, cf. Fig. 4.

$$\Lambda(e) = \left(k_P + k_I \frac{1}{s} + k_D \frac{s}{1 + T_N s} \right) e(s) \tag{9}$$

Adding the controller Eq. (9) to the model-based feedforward control voltage v_d with Eq. (10), we achieve tracking the operating point with the controller correcting the open-loop model errors and external disturbances.

$$v^* = \Lambda(e) + v_d \tag{10}$$

The feedforward Eq. (11) for linear control is calculated similar to the open-loop control Eq. (8) by using Eq. (7).

$$v_d = \begin{cases} \sqrt{\dfrac{2 J u_d}{C_1'(\theta_d)}} & \text{for} \quad u_d > 0 \\[3mm] \sqrt{\dfrac{2 J u_d}{C_2'(\theta_d)}} & \text{for} \quad u_d \le 0 \end{cases} \tag{11}$$

Finally, the electrode comb selection is realized according to the sign of the control voltage v^*, Eq. (12).

$$v_1 = \begin{cases} v^* & \text{for} \quad v^* > 0 \\ 0 & \text{for} \quad v^* \le 0 \end{cases} \qquad\qquad v_2 = \begin{cases} 0 & \text{for} \quad v^* \ge 0 \\ v^* & \text{for} \quad v^* < 0 \end{cases} \tag{12}$$
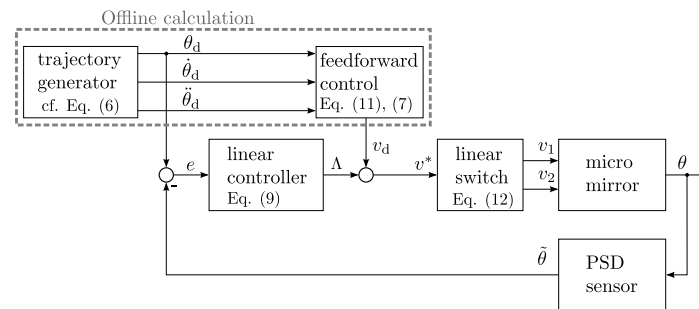

Figure 4: Linear control structure

3.2 Flatness-based control

The given nonlinear system, Eq. (4), satisfies the property of *differential flatness* [17, 18], that was proved in [3], using the flat output $y := x_1 = \theta$. Flat systems are a subclass of globally invertible systems [19]. The flatness-based nonlinear feedback control stabilizes the system state $\boldsymbol{x}$ with the position error $e = \theta_d - \tilde{\theta}$ and the velocity error $\dot{e} = \dot{\theta}_d - \dot{\tilde{\theta}}$, by adding the stabilizing feedback $\Lambda(e, \dot{e})$ to the feedforward control u_d. Consequently, we define the new input u^* Eq. (13):

$$u^* = \Lambda(e, \dot{e}) + u_d \tag{13}$$

For further information contact: schroedter@acin.tuwien.ac.at, https://orcid.org/0000-0003-3259-4571

The system model Eq. (4) has two independent states, that can be stabilized using the following error definition: $\Lambda := k_\mathrm{P}e + k_\mathrm{D}\dot{e} \rightarrow 0$, cf. [20]. We implement an additional integrator term to eliminate potentially remaining control deviations and get Eq. (14).

$$\Lambda(e,\dot{e}) = k_\mathrm{P}e + k_\mathrm{D}\dot{e} + k_\mathrm{I}\int_0^t e(t')\mathrm{d}t' \tag{14}$$

Compared to the linear control, the nonlinear (flatness-based and sliding-mode, see next paragraph) control structures consider the electrostatic nonlinearities in the nonlinear switch using the observed mirror position $\hat{\theta}$ with Eq. (15). The nonlinear control structure is shown in Fig. 5.

$$v_1 = \begin{cases} \sqrt{\dfrac{2Ju^*}{C_1'(\hat{\theta})}} & \text{for} \quad u^* > 0 \\ 0 & \text{for} \quad u^* \leq 0 \end{cases} \qquad v_2 = \begin{cases} 0 & \text{for} \quad u^* > 0 \\ \sqrt{\dfrac{2Ju^*}{C_2'(\hat{\theta})}} & \text{for} \quad u^* \leq 0 \end{cases} \tag{15}$$
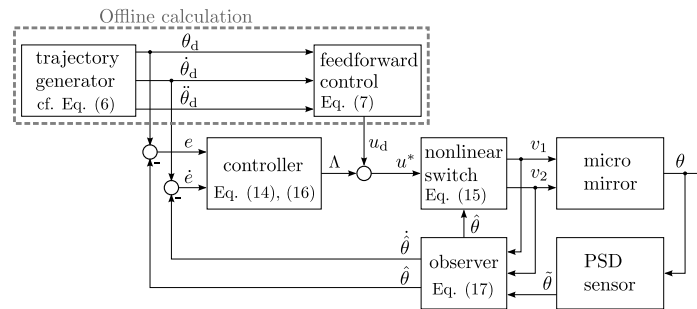

Figure 5: Nonlinear control structure (flatness-based control and sliding-mode control)

3.3 Sliding-mode control

We implement the sliding-mode control [10, 11] Eq. (16) by adding the gain q with the sign of the hypersurface to the flatness-based controller Eq. (14). The control structure is equivalent to flatness-based control, cf. Fig. 5.

$$\Lambda(e,\dot{e}) = k_\mathrm{P}e + k_\mathrm{D}\dot{e} + k_\mathrm{I}\int_0^t e(t')\mathrm{d}t' + q \cdot \mathrm{sign}\underbrace{\left(r_1\int_0^t e(t')\mathrm{d}t' + r_2 e + \dot{e}\right)}_{s} \tag{16}$$

The hypersurface $s(\int e, e, \dot{e})$ describes a sliding surface defined with the constants r_1, r_2 on which the control errors pass along to decrease the tracking error. The sign function leads to chattering of the control output Λ. Chattering usually results in increased actuator wear due to high frequency actuator motion. As the electrostatic comb drive operates without frictional connections, chattering does not limit the actuator functionality.

3.4 Observer design

As the angular velocity $\dot{\theta}$ cannot be measured directly, we design an observer to estimate the system state $\hat{\boldsymbol{x}}$. The observer Eq. (17) represents a virtual copy of the system Eq. (4) applying the same inputs v_1, v_2 and the same output $y = \theta$. The additional correction term $\boldsymbol{K}\hat{e}$ adapts the estimated system state $\hat{\boldsymbol{x}}$ towards the real measured mirror output $\tilde{\theta}$ using observer gain $\boldsymbol{K} = (\kappa_1, \kappa_2)^T$ and observing error $\hat{e} = \hat{\theta} - \tilde{\theta}$.

$$\dot{\hat{\boldsymbol{x}}} = \underbrace{\begin{pmatrix} 0 & 1 \\ 0 & -\frac{b}{J} \end{pmatrix}}_{\boldsymbol{A}}\hat{\boldsymbol{x}} + \underbrace{\begin{pmatrix} 0 \\ 1 \end{pmatrix}}_{\boldsymbol{B}}w + \boldsymbol{K}\hat{e} \qquad\qquad y = \underbrace{\begin{pmatrix} 1 & 0 \end{pmatrix}}_{\boldsymbol{C}^T}\hat{\boldsymbol{x}} \tag{17}$$

For further information contact: schroedter@acin.tuwien.ac.at, https://orcid.org/0000-0003-3259-4571

The observer dynamics is parameterized by placing the two observer poles with Eq. (18) at identical real frequencies applying the ACKERMANN formula [21].

$$\det\left[s\boldsymbol{I} - \left(\boldsymbol{A} - \boldsymbol{K}\boldsymbol{C}^T\right)\right] = s^2 + \kappa_1 s + \kappa_2 \tag{18}$$

We test two variants for the new input w, Eq. (19), resulting in two observers: the *normal form* observer, Fig. 6a, using the measured deflection $\tilde{\theta}$ and the *High-Gain* observer [22], Fig. 6b, using the estimated deflection $\hat{\theta}$, for evaluating the nonlinear spring torque τ_s.

$$\text{Normal form observer}: \qquad w = \alpha(\tilde{\theta}, v_1, v_2) = u - \frac{1}{J}\tau_\mathrm{s}(\tilde{\theta}) \tag{19a}$$

$$\text{High-Gain observer}: \qquad w = \alpha(\hat{\theta}, v_1, v_2) = u - \frac{1}{J}\tau_\mathrm{s}(\hat{\theta}) \tag{19b}$$

(a) Normal form observer Eq. (19a) with measurement $\tilde{\theta}$ for model prediction

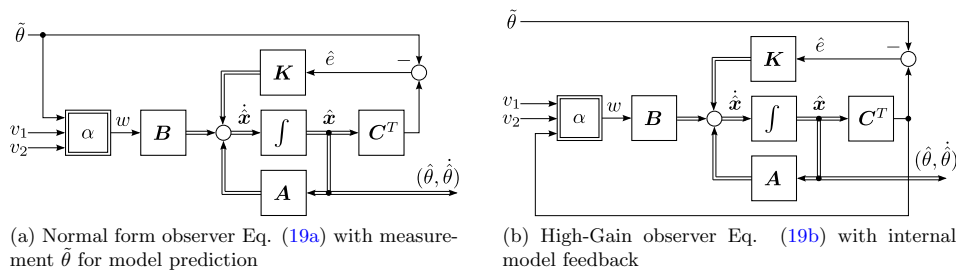(b) High-Gain observer Eq. (19b) with internal model feedback

Figure 6: Observer structures for normal form and High-Gain observer

The experimental and simulative comparison of both observers demonstrates a similar behavior, see Fig. 7. We find the lowest observer errors at an absolute pole frequency between 1 kHz and 3 kHz. However the High-Gain observer shows a smaller error for observer pole frequencies below 1kHz. Therefore, we subsequent apply the favorite High-Gain observer for the experimental validation in section 4.

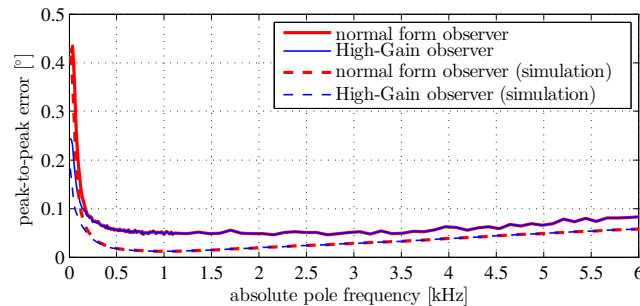Figure 7: Observer error $\hat{e} = \hat{\theta} - \tilde{\theta}$ (absolute peak-to-peak error of 200 periods), comparing normal form and High-Gain observer with open-loop control for a 50 Hz triangle trajectory as shown in Fig. 10b: measured data are illustrated with straight line and MATLAB/SIMULINK® simulation (including noise of $\sigma_\mathrm{PSD} = 6.36\,\mathrm{m}°$) data with dashed line

4. EXPERIMENTAL VALIDATION

4.1 Real-time setup

The experimental validation is performed with the setup shown in Fig. 8. All online calculations are processed with 40kHz on the real-time controller DS1007 from dSPACE®, that is piloted by a host computer. The controller output signals are delivered as low voltage signal v_1^*, v_2^* with the DA-converter DS2102 and then amplified with a 50x high-voltage amplifier from TEGAM® to the desired drive voltages v_1, v_2. For measuring the mirror tilt angle we apply the laser beam deflected by the micro scanning mirror on a position sensitive device (PSD). The PSD displacement currents are converted to the sum v_{PSD}^+ and difference v_{PSD}^- voltages and digitalized by the AD-converter DS2004. The actual deflection angle is finally calculated using Eq. (20), where l_{PSD} specifies the PSD size and k_{PSD} denotes a calibration factor.
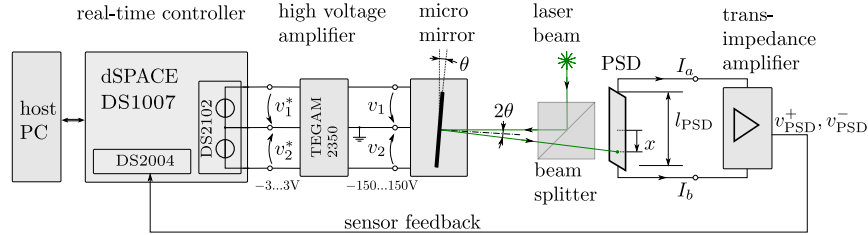

Figure 8: Experimental setup with real-time controller, 50x high-voltage amplifier and micro mirror tilt angle measurement via PSD for control feedback

$$\tilde{\theta} = \frac{1}{2}\arctan\left(\frac{l_{PSD}}{k_{PSD}}\frac{v_{PSD}^-}{v_{PSD}^+}\right) \tag{20}$$

4.2 Experimental results

First, we validate the presented control methods with a *step response* to $5°$, i.e. half of the maximum deflection, as shown in Fig. 9. The closed-loop setup receives a true step as an input signal. For all three closed-loop methods, we determine a valuable settling time within 0.1% of steady state deflection in about $3\,\text{ms}$, cf. Tab. 1 with the fastest result using sliding-mode control. The control parameter are tuned manually. For open-loop control the identical control reference will lead to excessive oscillation, as we have previously shown [8]. To enable a clear comparison we have designed a smooth step with $5\,\text{ms}$ rise time as input signal for open loop control, using the polynomials Eq. (6). We see in Fig. 9 that the settling time is not only limited by this rise time but also by remaining oscillatory motion. The result is a settling time in the order of $500\,\text{ms}$.

Table 1: Settling time for step response to $5°$ within 0.1% from Fig. 2: smooth step designed with $5\,\text{ms}$ for open-loop control and discontinuous step for closed-loop control

	settling time within 0.1%
open-loop	$484.9\,\text{ms}$
linear closed-loop control	$3.65\,\text{ms}$
flatness-based closed-loop control	$3.28\,\text{ms}$
sliding-mode closed-loop control	$2.9\,\text{ms}$

For raster scanning the quasistatic axis requires performing a triangle or sawtooth shaped trajectory. While the triangle trajectory features an overall shorter reversal time, the sawtooth trajectory has a beneficial advantage in data processing concerning blurring effects, because the scan pattern keeps up the same direction [23, 24]. To better interpret the tracking performance, let us define the following errors, Eq. (21).
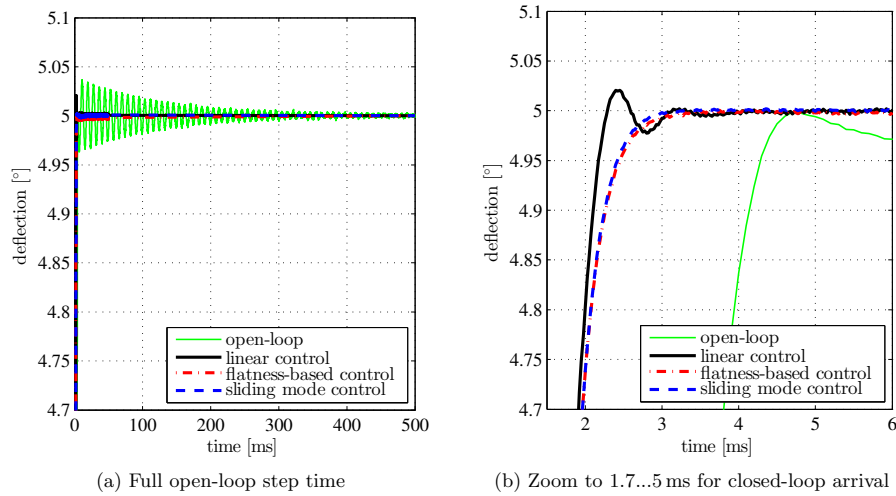
For further information contact: schroedter@acin.tuwien.ac.at, https://orcid.org/0000-0003-3259-4571

(a) Full open-loop step time

(b) Zoom to 1.7...5 ms for closed-loop arrival

Figure 9: Step response to $5\,°$ with smooth step designed with $5\,\mathrm{ms}$ rise time for open-loop control and discontinuous step for closed-loop control strategies, cf. settling times in Tab. 1, using the control parameters for linear control: $k_\mathrm{P} = 6.5 \times 10^3$, $k_\mathrm{I} = 0$, $k_\mathrm{D} = 7.9$, $T_\mathrm{N} = 1/4000\,\mathrm{s}$; for flatness-based control: $k_\mathrm{P} = 4 \times 10^6$, $k_\mathrm{I} = 0$, $k_\mathrm{D} = 4000$, $f_\mathrm{obs} = 6f_0$; for sliding-mode control: $k_\mathrm{P} = 4 \times 10^6$, $k_\mathrm{I} = 3 \times 10^7$, $k_\mathrm{D} = 4000$, $f_\mathrm{obs} = 6f_0$, $q = 500$

Error definition   This error analysis aims at neglecting the PSD noise of about $\sigma_\mathrm{PSD} = 6.36\,\mathrm{m}°$ and detecting the real mirror deflection. We define the mean error $\overline{e}(t)$, Eq. (21a), that denotes the error between the desired θ_d and the measured deflection $\tilde{\theta}$, evaluating 200 consecutive periods with a period time of $T = \frac{1}{f}$, where f is the scan frequency. Subsequently, we compare the percentaged peak-to-peak value $\Delta\overline{e}$ of the mean error as specified with Eq. (21b).

$$\text{mean error:} \quad \overline{e}(t) = \frac{1}{200} \sum_{i=1}^{200} \left(\theta_\mathrm{d}(t) - \tilde{\theta}_i(t) \right), \quad t = 0...T \tag{21a}$$

$$\text{peak-to-peak mean error [\%]:} \quad \Delta\overline{e} = \frac{\max\left(\overline{e}\right) - \min\left(\overline{e}\right)}{2\theta_\mathrm{max}} \cdot 100 \tag{21b}$$

The command *triangle* trajectories in Fig. 10a,10b are conditioned with $10\,\%$ reserve of the maximum drive torque towards the required drive torque, resulting in $\theta_\mathrm{lin} = 9.16\,°$ for $10\,\mathrm{Hz}$ and $\theta_\mathrm{lin} = 8.79\,°$ for $50\,\mathrm{Hz}$ scan frequency. Regarding the control mean error in Fig. 10c,10d, we recognize a higher deviation during the reversal times, that is caused by the torque added to change the mirror direction. The command *sawtooth* trajectories in Fig. 11a,11b are designed with in $\theta_\mathrm{lin} = 9.5\,°$ for $10\,\mathrm{Hz}$ and $\theta_\mathrm{lin} = 9\,°$ for $50\,\mathrm{Hz}$ scan frequency.

Comparing the control results shown in Fig. 10,11 and summarized in Tab. 2, we evaluate the highest performance with the flatness-based control for most test trajectories, except the $10\,\mathrm{Hz}$ sawtooth, where the sliding-mode control has smaller errors, but shows an offset towards zero deflection within the linear area. Nevertheless the linear control demonstrates a comparable low error for the $50\,\mathrm{Hz}$ sawtooth trajectory, Fig. 11b. Furthermore, let us point out the 1.3 to 3.6 times higher errors for the $50\,\mathrm{Hz}$ trajectory in Tab. 2 compared to the $10\,\mathrm{Hz}$ trajectory, that originate from the amplitude increase due to the mirror's resonance frequency at $f_0 = 113.3\,\mathrm{Hz}$. Finally, the control parameter choice is essential for the optimal performance.

For further information contact: schroedter@acin.tuwien.ac.at, https://orcid.org/0000-0003-3259-4571

Table 2: Summarized measurement results of Fig. 10,11 with peak-to-peak mean error $\Delta\bar{e}$, Eq. (21b) in the linear area, for triangle and sawtooth trajectory with 10 Hz and 50 Hz and $\theta_{\max} = 10°$

| trajectory type	triangle		sawtooth	
trajectory frequency	10 Hz	50 Hz	10 Hz	50 Hz
$\Delta\bar{e}$ for linear control	0.112 %	0.295 %	0.109 %	0.142 %
$\Delta\bar{e}$ for flatness-based control	0.078 %	0.271 %	0.077 %	0.141 %
$\Delta\bar{e}$ for sliding-mode control	0.130 %	0.433 %	0.052 %	0.169 %
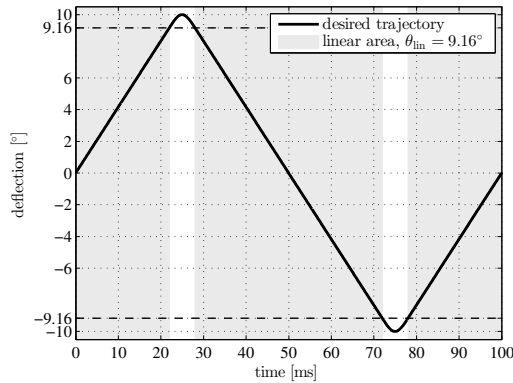
(a) 10 Hz *triangle* command trajectory with linear area (gray shaded) between $\pm\theta_{\mathrm{lin}} = 9.16°$
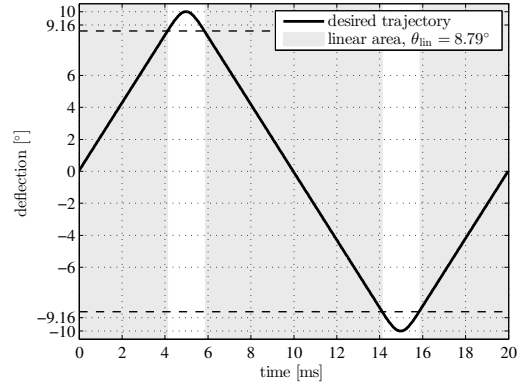
(b) 50 Hz *triangle* command trajectory with linear (gray shaded) area between $\pm\theta_{\mathrm{lin}} = 8.79°$
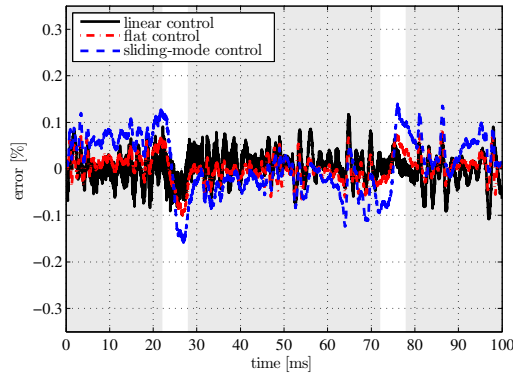
(c) Mean control error $\bar{e}(t)$ of 200 periods in percent of max. deflection $\theta_{\max} = 10°$ for 10 Hz *triangle* trajectory (Fig. 10a) using the following parameters for linear control: $k_{\mathrm{P}} = 5000$, $k_{\mathrm{I}} = 0$, $k_{\mathrm{D}} = 2$, $T_{\mathrm{N}} = 1/3000$ s; for flatness-based control: $k_{\mathrm{P}} = 2 \times 10^7$, $k_{\mathrm{I}} = 0$, $k_{\mathrm{D}} = 5000$, $f_{\mathrm{obs}} = 6f_0$; for sliding-mode control: $k_{\mathrm{P}} = 2 \times 10^7$, $k_{\mathrm{I}} = 0$, $k_{\mathrm{D}} = 2000$, $f_{\mathrm{obs}} = 4f_0$, $q = 2000$
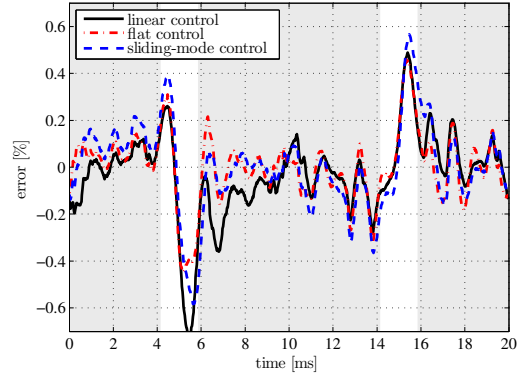
(d) Mean control error $\bar{e}(t)$ of 200 periods in percent of max. deflection $\theta_{\max} = 10°$ for 50 Hz *triangle* trajectory (Fig. 10b) using the following parameters for linear control: $k_{\mathrm{P}} = 2000$, $k_{\mathrm{I}} = 0$, $k_{\mathrm{D}} = 7$, $T_{\mathrm{N}} = 1/4000$ s; for flatness-based control: $k_{\mathrm{P}} = 4 \times 10^7$, $k_{\mathrm{I}} = 0$, $k_{\mathrm{D}} = 3000$, $f_{\mathrm{obs}} = 6f_0$; for sliding-mode control: $k_{\mathrm{P}} = 4 \times 10^7$, $k_{\mathrm{I}} = 0$, $k_{\mathrm{D}} = 2000$, $f_{\mathrm{obs}} = 4f_0$, $q = 2000$

Figure 10: Measurement results for real-time control on *triangle* 10 Hz and 50 Hz trajectory using linear, flatness-based and sliding-mode control
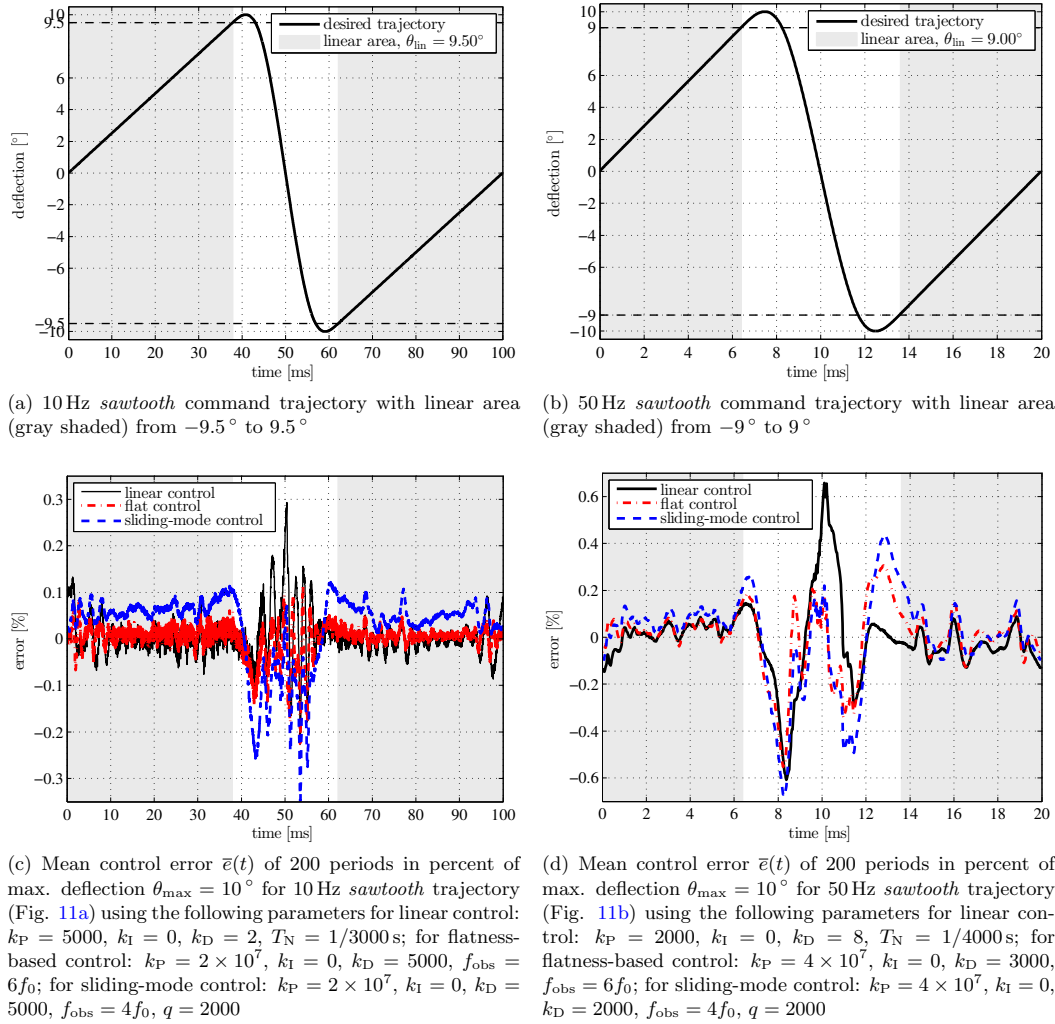
(a) 10 Hz *sawtooth* command trajectory with linear area (gray shaded) from $-9.5°$ to $9.5°$

(b) 50 Hz *sawtooth* command trajectory with linear area (gray shaded) from $-9°$ to $9°$

(c) Mean control error $\overline{e}(t)$ of 200 periods in percent of max. deflection $\theta_{max} = 10°$ for 10 Hz *sawtooth* trajectory (Fig. 11a) using the following parameters for linear control: $k_P = 5000$, $k_I = 0$, $k_D = 2$, $T_N = 1/3000\,\mathrm{s}$; for flatness-based control: $k_P = 2 \times 10^7$, $k_I = 0$, $k_D = 5000$, $f_{obs} = 6f_0$; for sliding-mode control: $k_P = 2 \times 10^7$, $k_I = 0$, $k_D = 5000$, $f_{obs} = 4f_0$, $q = 2000$

(d) Mean control error $\overline{e}(t)$ of 200 periods in percent of max. deflection $\theta_{max} = 10°$ for 50 Hz *sawtooth* trajectory (Fig. 11b) using the following parameters for linear control: $k_P = 2000$, $k_I = 0$, $k_D = 8$, $T_N = 1/4000\,\mathrm{s}$; for flatness-based control: $k_P = 4 \times 10^7$, $k_I = 0$, $k_D = 3000$, $f_{obs} = 6f_0$; for sliding-mode control: $k_P = 4 \times 10^7$, $k_I = 0$, $k_D = 2000$, $f_{obs} = 4f_0$, $q = 2000$

Figure 11: Measurement results for real-time control on *sawtooth* 10 Hz and 50 Hz trajectory using linear, flatness-based and sliding-mode control

For further information contact: schroedter@acin.tuwien.ac.at, https://orcid.org/0000-0003-3259-4571

5. SUMMARY

In this contribution we have validated the real-time closed-loop control for the quasistatic axis of a 2D micro scanner with a novel electrostatic SVC drive intending raster scan applications. In the experimental validation we achieve about $3\,\mathrm{ms}$ settling time for a step response to $5\,^\circ$ deflection. Furthermore we tested triangle and sawtooth trajectories with a max. deflection of $10\,^\circ$ featuring very low tracking errors of about $0.1\,\%$ for $10\,\mathrm{Hz}$ and about $0.15\,\%$ to $0.3\,\%$ for $50\,\mathrm{Hz}$. Regarding the closed-loop control with an error of $0.078\,\%$ for a $10\,\mathrm{Hz}$ triangle trajectory, cf. Tab. 2, and the former open-loop errors $1.4079\,\%$ [1][*] and $1.456\,\%$ [3][†], we have improved the control performance by factor 18. The comparison of the linear and two nonlinear control strategies yield the best performance with the flatness-based control structure for most test cases. Nevertheless the linear control stays a relevant candidate for an analog realization, that is prospectively required for mirrors with high eigenfrequencies above $10\,\mathrm{kHz}$. Moreover, in the nonlinear control methods the High-Gain observer shows an advantageous behavior for small observer gains, compared to the normal form observer.

6. OUTLOOK

Integrated piezo-resistive sensors enable system operation without need for an external sensor, resulting in a system design with smaller package density and lower cost. The on-chip piezo-resistive sensor [15, 16] was depicted with high noise and unserviceable as a feedback sensor for the demonstrated device, cf. Fig. 1b. Recent developments [13] have optimized the signal quality and now will allow a feasible position feedback for the closed-loop control methods as presented in this paper.

REFERENCES

[1] Schroedter, R., Janschek, K., and Sandner, T., "Jerk and Current Limited Flatness-based Open Loop Control of Foveation Scanning Electrostatic Micromirrors," in [*International Federation of Automation and Control (IFAC) Conference, 24-29 August 2014, Cape Town, South Africa*], 2685–2690 (2014).

[2] Schroedter, R., Roth, M., Sandner, T., and Janschek, K., "Modellgestützte Bewegungsführung von quasistatischen Mikroscannern (Model-based motion tracking for quasistatic microscanners)," in [*Tagungsband Fachtagung Mechatronik 2013, Aachen, 06.03.-08.03.2013*], 141–146 (2013).

[3] Janschek, K., Schroedter, R., and Sandner, T., "Flatness-based open loop command tracking for quasistatic microscanners," *ASME Dynamic Systems and Control Conference (DSCC) 2013, Stanford University, CA, USA* **3**(WeAT3.1), V003T37A001, 5 pages (2013).

[4] Scholles, M., Bräuer, A., Frommhagen, K., Gerwig, C., Lakner, H., Schenk, H., and Schwarzenberg, M., "Ultracompact laser projection systems based on two-dimensional resonant microscanning mirrors," *Journal of Micro/Nanolithography, MEMS, and MOEMS* **7**(2), 021001–021001–11 (2008).

[5] Wolter, A., Hsu, S.-T., Schenk, H., and Lakner, H. K., "Applications and requirements for MEMS scanner mirrors," *Proc. SPIE* **5719**, 64–75 (2005).

[6] Kenda, A., Kraft, M., Tortschanoff, A., Scherf, W., Sandner, T., Schenk, H., Lüttjohann, S., and Simon, A., "Development, characterization and application of compact spectrometers based on MEMS with in-plane capacitive drives," *Proc. SPIE* **9101**, 910102–910102–10 (2014).

[7] Sandner, T., Grasshoff, T., Wildenhain, M., and Schenk, H., "Synchronized microscanner array for large aperture receiver optics of LIDAR systems," in [*MOEMS and Miniaturized Systems IX*], Harald Schenk, W. P., ed., *Proc. SPIE* **7594**, 75940C–75940C–12 (2010).

[8] Janschek, K., Sandner, T., Schroedter, R., and Roth, M., "Adaptive Prefilter Design for Control of Quasistatic Microscanners," in [*Proceedings of 6th IFAC Symposium on Mechatronic Systems 2013, Hangzhou, China*], Bingfeng, J., ed., 197–206 (Apr 2013).

[9] Janschek, K., [*Mechatronic Systems Design - Methods, Models, Concepts*], Springer (2012).

[10] Khalil, H. K., [*Nonlinear systems*], vol. 3, Prentice Hall, New Jersey (2002).

[11] Utkin, V., Guldner, J., and Shi, J., [*Sliding Mode Control in Electro-Mechanical Systems, Second Edition*], Automation and Control Engineering, CRC Press (2009).

---

[*]Result from [1, Tab. 1] using $80\,\%$ linear area with regard to maximum deflection of $7\,^\circ$ according Eq. (21b)

[†]Result from [3, Tab. 1] adapted with factor $12.8\,^\circ/16\,^\circ$ relating to maximum deflection of $8\,^\circ$

[12] Adamy, J., [*Nichtlineare Regelungen*], Springer (2009).

[13] Grahmann, J., Dreyhaupt, A., Drabe, C., Schroedter, R., Kamenz, J., Herrmann, A., and Sandner, T., "MEMS-mirror based trajectory resolution and precision enabled by two different piezoresistive sensor technologies," in [*MOEMS and Miniaturized Systems XV*], *Proc. SPIE* (2016). to be published.

[14] Thielemann, J., Sandner, T., Schwarzer, S., Cupcic, U., Schumann-Olsen, H., and Kirkhus, T., "Taco: Threedimensional camera with object detection and foveation." www.taco-project.eu (2010). EC FP7 grant no 248623.

[15] Sandner, T., Conrad, H., Klose, T., and Schenk, H., "Integrated Piezo-resistive Position sensor for Microscanning Mirrors," in [*Optical MEMS and Nanophotonics, 2007 IEEE/LEOS International Conference on*], Harald Schenk, W. P., ed., 195–196 (Aug 2007).

[16] Grahmann, J., Conrad, H., Sandner, T., Klose, T., and Schenk, H., "Integrated position sensing for 2D microscanning mirrors using the SOI device layer as the piezoresistive mechanical-elastic transformer," in [*MOEMS and Miniaturized Systems VIII*], *Proc. SPIE* **7208**, 720808–720808–10 (2009).

[17] Fliess, M., J., L., P., M., and Rouchon, P., "On differentially flat nonlinear systems," in [*Nonlinear Control System Design*], Fliess, M., ed., 408–412, Pergamon Press (1992).

[18] Fliess, M., Lévine, J., Martin, P., and Rouchon, P., "Flatness and defect of non-linear systems: introductory theory and examples," *International journal of control* **61**(6), 1327–1361 (1995).

[19] Isidori, A., [*Nonlinear control systems*], Springer (1995).

[20] Levine, J., [*Analysis and control of nonlinear systems: A flatness-based approach*], Springer (2009).

[21] Röbenack, K., "Computation of the observer gain for extended Luenberger observers using automatic differentiation," **21**(1), 33–47 (2004).

[22] Röbenack, K. and Lynch, A., "High-gain nonlinear observer design using the observer canonical form," *Control Theory Applications, IET* **1**, 1574–1579 (November 2007).

[23] Duma, V.-F., sung Lee, K., Meemon, P., and Rolland, J. P., "Experimental investigations of the scanning functions of galvanometer-based scanners with applications in oct," *Appl. Opt.* **50**, 5735–5749 (Oct 2011).

[24] Marshall, G. F., [*Handbook of optical and laser scanning*], Marcel Dekker, Inc. (2004).